International Journal of Heat and Fluid Flow 71 (2018) 200–209

Contents lists available at ScienceDirect

International Journal of Heat and Fluid Flow

journal homepage: www.elsevier.com/locate/ijhff

A modified Parametric Forcing Approach for modelling of roughness

Pourya Forooghi*[,a], Bettina Frohnapfel[a], Franco Magagnato[a], Angela Busse[b]

[a] Institute of Fluid Mechanics, Karlsruhe Institute of Technology, Kaiserstraße 10, Karlsruhe 76149, Germany
[b] School of Engineering, University of Glasgow, Glasgow G12 8QQ, UK

ARTICLE INFO

Keywords:
Roughness modelling
Parametric forcing
Turbulent channel flow

ABSTRACT

Surface roughness in turbulent channel flow is effectively modelled using a modified version of the Parametric Forcing Approach introduced by Busse and Sandham (2012). In this modified approach, the model functions are determined based on the surface geometry and two model constants, whose value can be fine tuned. In addition to a quadratic forcing term, accounting for the effect of form drag due to roughness, a linear forcing term, analogous to the Darcy term in the context of porous media, is employed in order to represent the viscous drag. Comparison of the results with full-geometry resolved Direct Numerical Simulation (DNS) data for the case of dense roughness (frontal solidity ≅0.4) shows a satisfactory prediction of mean velocity profile, and hence the friction factor, by the model. The model is found to be able to reproduce the trends of friction factor with morphological properties of surface such as skewness of the surface height probability density function and coefficient of variation of the peak heights.

1. Introduction

Study of turbulent flows over rough surfaces finds application in several engineering – e.g. turbomachinery, marine transportation and ice accretion on aircrafts – and geophysical – e.g. wind flow over plant and urban canopies – problems. Roughness causes an increase in the friction factor.

$$C_f = \frac{\tau_w}{\frac{1}{2}\rho U_b^2} \tag{1}$$

In Eq. (1) τ_w and U_b denote wall shear stress and bulk velocity. It is also well established that roughness leads to a shift ΔU^+ in the logarithmic law of the wall (Nikuradse, 1933; Hama, 1954).

$$U^+(y) = \frac{1}{\kappa} ln(y^+) + 5.5 - \Delta U^+ \tag{2}$$

where $\kappa = 0.4$ is the von Kármán constant and the value 5.5 is the log-law intercept for a smooth wall. It can be shown that an increase in the roughness function ΔU^+ corresponds to an increase in friction factor (Jimenez, 2004; Flack and Schultz, 2010).

Alternatively, Eq. (2) can be written as

$$U^+(y) = \frac{1}{\kappa} ln\left(\frac{y}{k_s}\right) + 8.5 \tag{3}$$

where roughness function ΔU^+ is replaced by the interchangeably usable quantity k_s – effective or equivalent sand-grain roughness height (Jimenez, 2004). For a majority of practical rough surfaces (so called k-type roughness), k_s is "proportional to the dimensions of roughness elements", provided that the roughness elements are large enough to fall into the 'fully-rough' regime (Jimenez, 2004). The ratio of k_s to the physical characteristic dimension k of roughness is a function of the surface geometry (Jimenez, 2004). A comprehensive review on the dependence of the ratio k_s/k on different geometrical surface parameters has been undertaken by Flack and Schultz (2010). Recently, Forooghi et al. (2017) and Thakkar et al. (2017) investigated several irregular rough surfaces using DNS in order to determine the most important surface parameters for the prediction of flow properties, i.e. ΔU^+ or k_s. There is a consensus among above references that, at constant roughness density, flow properties are most sensitive to the skewness Sk of the surface height probability distribution function. Surface slope also plays an important role in determining both skin friction and physics of the flow. With a decrease in effective slope – defined as mean absolute streamwise surface slope – form drag loses its dominance in the momentum exchange between the surface and flow (Napoli et al., 2008; Schultz and Flack, 2009).

DNS in which the details of surface geometry are resolved is required to guarantee that both roughness and flow scales are properly accounted for. A number of such simulations have been published in the past, in which the surface geometry is captured either by body conforming grids (Choi et al., 1993; Chan et al., 2015) or immersed boundary method (IBM) (Orlandi and Leonardi, 2006; Bhaganagar, 2008; Busse et al., 2015; Forooghi et al., 2017; Mazzuoli and Uhlmann,

* Corresponding author.
E-mail address: forooghi@kit.edu (P. Forooghi).

https://doi.org/10.1016/j.ijheatfluidflow.2018.03.019
Received 8 November 2017; Received in revised form 29 March 2018; Accepted 29 March 2018
Available online 13 April 2018

2017). Both approaches are extremely demanding in terms of computational cost and/or grid generation effort. A way to avoid such difficulties is using a modified version of the Navier–Stokes equation near the wall, in which roughness is 'effectively' modelled. These models, clearly, do not process the degree of fidelity that full-surface resolved DNS provides, thus, require careful verification. In the framework of Reynolds-averaged Navier–Stokes, for instance, so-called Discrete Element Method (DEM) has been used for a long time (Taylor et al., 1985; Tarada, 1990). In DEM, roughness geometry is represented by simple roughness elements and the mass and momentum conservation equations are averaged over control volumes containing several of these elements. Effects of form drag and vortex shedding from roughness elements enter the momentum and turbulent kinetic energy equations through source terms; consequently, not only the momentum equation but also turbulence transport equations contain extra 'modelled' terms.

The idea of modifications in Navier–Stokes equation for roughness modelling has also been used in LES and DNS context. Cui et al. (2003) suggested an approach in which an arbitrary rough surface is decomposed into two parts: resolved scale and sub-grid scale roughness, for the former immersed boundary method and for the latter a random body-force model is used. For very high Reynolds numbers where the roughness height falls below the first near-wall grid point, Anderson and Meneveau (2010) suggested an LES model in which a body force is applied within the first grid-point. The value of the body force is determined based on total incoming momentum flux into the roughness.

Busse and Sandham (2012) proposed a Parametric Forcing Approach (PFA) in which the effect of roughness is introduced by adding the body force term $-\alpha_i F_i(y) u_i|u_i|$ to the otherwise-unchanged Navier–Stokes equation (no summation over index i). u_i denotes instantaneous velocity and $i = 1, 2, 3$ indicate streamwise, wall-normal and spanwise directions corresponding to x, y, z coordinates, respectively. α_i and $F_i(y)$ are referred to as 'roughness factor' and 'roughness shape function' by these authors, respectively. They further simplify the model by applying $\alpha_1 F_1 = \alpha_3 F_3 = \alpha F$ and $\alpha_2 = 0$. By using a DNS grid, PFA involves no other modelling except for the forcing term that represents the momentum exchange between the flow and roughness, therefore, it is possible to purely evaluate the performance of roughness modelling terms. In the PFA introduced in Busse and Sandham (2012) the function αF is not directly related to a specific roughness geometry, therefore, cannot be determined a priori.

The present work aims at a modified version of PFA, in which – apart from the tunable scalar model constants – the forcing amplitude can be determined a priori for a desired roughness geometry, so that the mean flow profile and, thus, the 'friction factor' can be predicted correctly. The model is expected to satisfactorily capture the trends of friction factor with two important topographical surface parameters, i.e. 'skewness' and 'coefficient of variation of roughness peak heights'. Full-geometry resolved DNS data from Forooghi et al. (2017) is used to evaluate the model and its capability to follow the physical trends.

2. Roughness samples

Four roughness samples with systematically chosen geometrical surface parameters are considered in the present paper. The full-geometry resolved DNS for these surfaces have been reported by Forooghi et al. (2017); in the present work the 'geometrical functions' required in the modified PFA (details in Section 3) are calculated for the same samples and the results are compared. The geometry of roughness is generated using an algorithm explained in full in Forooghi et al. (2017), which creates 3D irregular rough surfaces $\tilde{k}(x, z)$. Briefly, the geometry is generated by mounting axisymmetric roughness elements with prescribed shape and spacing in a random pattern on a smooth 'reference plane' which is the lower boundary of the computational domain. Certain topographical properties of the roughness can be adjusted in this approach. Before discussing these properties, it should be stressed that in the present study we focus on the roughness elements with high slopes. As discussed in the introduction, a rough surface with low slope does not behave in the same way as 'normal' roughness does. Schultz and Flack (2009) showed that when the surface slope falls below a certain threshold, the effective roughness height does not scale with the physical dimensions of roughness; therefore, they proposed calling this type of surfaces 'wavy' instead of 'rough'. These authors also suggested a threshold of 0.35 for the effective slope of a wavy surface. Yuan and Piomelli (2014), later on, found a considerably higher threshold equal to 0.7. The surfaces used in this work all have an effective slope equal to 0.88 which should be high enough to avoid any 'waviness' behaviour.

Table 1
Summary of surface samples used in the present study and the values of Reynolds number in the simulations. Results for cases *Ia, II* and *III* are discussed in details in Forooghi et al. (2017).

Sample	k/H	k_{MD}/H	Sk	Δ	k^+	Re_τ
Ia	0.12	0.074	0.21	0.7	67	498
Ib	0.06	0.037	0.21	0.7	32	500
II	0.12	0.047	0.66	0.7	64	502
III	0.19	0.1	0.21	0	110	499

As discussed in the introduction, data published in the literature suggest that, at a constant effective slope, skewness Sk defined as

$$Sk = \frac{1}{A \cdot k_{rms}^3} \int_A (\tilde{k} - k_{MD})^3 dA, \quad k_{rms}^2 = \frac{1}{A} \int_A (\tilde{k} - k_{MD})^2 dA \tag{4}$$

can control the effective roughness height to a high extent. In Eq. (4), A is the surface area projected on the reference plane, shortly wall-projected area, and k_{MD} (melt-down height) is the mean surface height. $\tilde{k}$, which is the surface height from the reference plane, is a function of coordinates in y-normal plane, i.e. $\tilde{k}(x, z)$. Forooghi et al. (2017) found that at constant skewness, a roughness composed of 'uniform' elements shows a higher resistance to flow than one with non-uniform elements. To measure the non-uniformity of the peak heights a 'coefficient of variation' Δ, defined as the height difference between the highest and the lowest peaks of the surface normalized with the mean peak height, is used.

Table 1 summarizes the geometrical properties of the surface samples. Sample *Ia* is used as the control case. Compared to this sample, sample *II* has a higher skewness but a similar Δ, while sample *III* has a similar Sk but its Δ is zero (uniform peak heights). Sample *Ib* has the same topographical properties as *Ia* but its dimensions are scaled down. Mean roughness peak height k[1] is halved in *Ib* compared to *Ia*. The values of k^+ shown in the table suggest that the studied surfaces likely span all the way between the transitionally-rough and fully-rough regimes, which facilitates assessing the versatility of the model under investigation.

The values of friction velocity Re_τ for each case – similar for the reference DNS and present simulations – are also listed in Table 1.

$$Re_\tau = \frac{u_\tau (H - k_{MD})}{\nu} \tag{5}$$

In Eq. (5), H is the distance between the bottom plane and the middle of the channel, i.e. the wall-normal dimension of the computational domain (see Section 4 for the complete description of the computational set-up), therefore, the length scale $(H - k_{MD})$ used in the definition of Reynolds number is the half-height of a channel with the same cross-section area or, namely, the 'effective' half-height of the channel. The friction velocity $u_\tau = (\tau_w/\rho)^{\frac{1}{2}}$ is based on the wall shear stress and is calculated from the integral momentum balance using the mean

[1] This quantity is used as the representative dimension of the roughness throughout the paper.

streamwise pressure gradient such that

$$\tau_w = -(dP/dx)\cdot(H - k_{MD}). \tag{6}$$

It should be noted that the wall shear stress calculated in this way takes into account contributions of both viscous friction and form drag on the roughness elements to the momentum transfer. In the present paper, all lengths and velocities in viscous units, denoted by plus subscript $()^+$, are nondimensionalized by u_τ and ν/u_τ, respectively.

3. Description of the model

In the present approach a 'forcing term' f_i is added to the incompressible momentum equation.

$$\frac{\partial u_i}{\partial t} + \frac{\partial u_i u_j}{\partial x_j} = -\frac{\partial p}{\partial x_i} + \nu\frac{\partial^2 u_i}{\partial x_j \partial x_j} + f_i \tag{7}$$

The forcing term acts parallel to the wall ($f_2 = 0$). Fig. 1 schematically illustrates the difference between the PFA and full-geometry resolved DNS. As indicated in the figure, the forcing term is non-zero everywhere below the plane of the highest roughness peak. The details of the rough surface are contained in the forcing term via 'geometrical functions' to be derived in the following.

As discussed in the introduction, Busse and Sandham (2012), among others, originally proposed a quadratic relation between the forcing term and local velocity. This kind of relation originates from the assumption that the form drag is the dominant resistance force due to roughness. The present DNS results (Forooghi et al., 2017) show, however, that when the roughness is dense, in the locations deep inside the roughness – i.e. the deepest valleys – the flow can be too slow for the form drag to be the only dominant force. In addition, it will be discussed further in Section 5 that it is not possible to satisfactorily match the mean velocity profiles from the reference DNS when merely a quadratic body force is used. These observations lend support to the idea that addition of a linear forcing term accounting for the viscous drag can improve the versatility of the model. Consequently, the forcing term will be the sum of a linear and a quadratic term

$$f_i = f_{L,i} + f_{Q,i} = -A(y)u_i - B(y)u_i|u_i|. \tag{8}$$

In Eq. 8, multiple index does not indicate summation. Comparing to the original (Busse and Sandham, 2012) formulation – disregarding the nondimensionalization – function $B(y)$ is the equivalent of $\alpha F(y)$ while $A(y)$ is zero in this reference.

One can identify a clear analogy between the present formulation and classical Darcy–Brinckmann–Forchheimer (DBF) equation for the modelling of flow in porous media (see reference Vafai and Kim, 1995), in which, a linear (Darcy) and a quadratic (Forchheimer) term are used to reproduce the effects of 'viscous' and 'inertial' resistance against the flow, respectively. While we do not necessarily intend to force a one-to-one correspondence between the present and the DBF formulations, it is clear that the analogy between the two can be beneficial in derivation of the forcing terms. In particular, when it comes to finding an expression for the linear forcing term, we find it reasonable to take the much elaborated Darcy term in the context of porous media as a starting point. Using this analogy, function A can be expressed as

$$A = \frac{\nu}{K} \tag{9}$$

where K is the 'permeability' of the porous medium. One of the most common approaches to the calculation of permeability in the context of porous media is the Kozney–Carman theory which utilizes the analogy between bundles of capillary conduits and porous media to derive an equation for K (Kaviany, 1995):

$$K = \frac{\epsilon d_h^2}{16 k_K} \tag{10}$$

where d_h is the 'pore' hydraulic diameter and ϵ is the porosity. k_K is a constant called 'Kozney constant' which contains the effects of solid shape and fluid flow path. A comprehensive review of the values of k_K for different porous media (ranging from artificial media made of in-line bars and cubes to real material such as soil and fluidized beds) performed by Ozgumus et al. (2014) reports values between roughly 4 and 16 for this constant. From the definition, the hydraulic diameter can be expressed as $d_h = \frac{4\epsilon}{s}$, s being total interface area per unit total volume. Replacing this expression into Eq. (10) and the result into Eq. (9) yields the following expression for the linear forcing amplitude function A:

$$A(y) = k_K \frac{\nu s(y)^2}{\epsilon(y)^3} \tag{11}$$

The dependency on the y-coordinate is necessary for roughness modelling as the geometrical properties of roughness vary considerably in the wall normal direction. Given the geometry of the roughness, one can find both ϵ and s functions at a certain y-position by integrating the fluid (void) volume and the interface area within an infinitesimally thin layer in y-direction which covers the entire domain in the wall-parallel plane. In general case, the dependency on the other two coordinates can also be included in the model to account for non-homogeneous roughness, but such a case is not discussed in the present paper to avoid complexity.

It should be mentioned that the Kozney–Carman theory is one of the possible approaches for the estimation of permeability used in the Darcy term. In the present work we adopt this approach due to its relative simplicity and familiarity, and we use k_K simply as a tunable model constant. For further refinements of the PFA model, further discussions on which permeability models may deliver best results will be beneficiary. Noteworthy is the possibility to evaluate the Darcy term directly by solving Stokes equations for a specific porous structure, as described in Lācis and Bagheri (2017), which rules out the model constant and leads to a fully a priori mode. Nevertheless, such a possibility is not examined in the present paper.

The quadratic forcing amplitude B in Eq. (8) can be found using the analogy to form drag of a bluff body:

$$B(y) = c_D \frac{s_f(y)}{2}. \tag{12}$$

where c_D can be seen as a type of drag coefficient and s_f is the total projected frontal surface area per unit total volume.

k_K and c_D are in fact the two model constant in the present formulation. Apart from these constants the model requires determining three 'geometrical functions' $\epsilon(y)$, $s(y)$ and $s_f(y)$. It should be mentioned that, the forcing term f_i as appears in Eqs. (7) and (8) is dimensional. One can consider nondimesionalization in viscous units

$$f_i^+ = \frac{f_i \cdot H}{u_\tau^2} \tag{13}$$

Consequently, the dimensionless form of the linear and quadratic forcing terms can be expressed as

$$f_{L,i}^+ = A^+ u_i^+, \quad A^+ = \frac{1}{Re_\tau}\frac{k_K s^{*2}}{\epsilon^3} \tag{14}$$

$$f_{Q,i}^+ = B^+ u_i^+ |u_i|^+, \quad B^+ = \frac{c_D s_f^*}{2} \tag{15}$$

where $s^* = s\cdot H$ and $s_f^* = s_f \cdot H$ are dimensionless geometrical functions; ϵ is by definition dimensionless. Constants k_K and c_D are also dimensionless. Obviously, any lengthscale other than H – for instance k – could alternatively be used for the nondimensionalization.

Tiles of $2H \times 2H$ area from the roughness geometries modelled in the present paper are shown in Fig. 2 along with the profiles of the dimensionless geometrical functions ϵ and s_f^*. Samples *Ia* and *Ib* are topographically identical; only in *Ib*, all dimensions of the roughness geometry are halved. It is observed in Fig. 2 (top) that both samples *I*

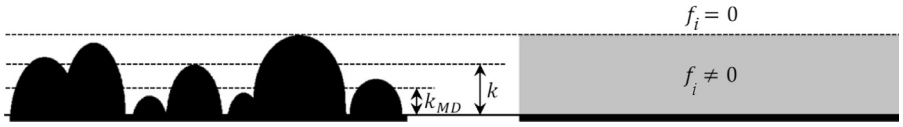

Fig. 1. Schematic representation of the PFA (right) against full-geometry resolved DNS (left). Details of the rough surface are 'homogenized' and effectively modelled through a forcing term f_i below the plane of the highest roughness peak (top dashed line). The other dashed lines in the figure schematically represent the plane of mean peak height ($y = k$) and the plane of mean surface height ($y = k_{MD}$).

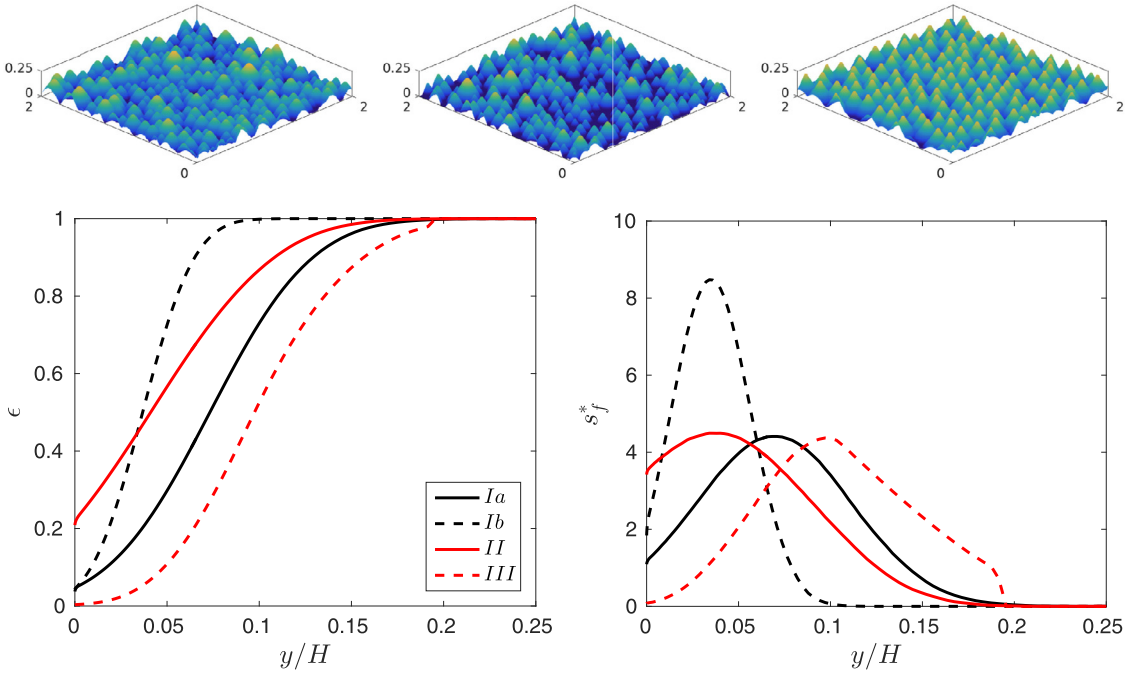

Fig. 2. Top: tiles of the surface samples modelled in the present paper from left to right *Ia, II* and *III* (all values shown on the figures are normalized by H; the surfaces are coloured with the local height for better visual distinction). Sample *Ib* is similar to *Ia*, scaled down in all dimensions by a factor 1/2. Bottom: geometrical functions ϵ (left) and s_f^* (right) for all surface samples. s^* is almost proportional to s_f^* hence not shown here for brevity.

and *III* (similarly *Ib*) consist of densely packed roughness elements while sample *II* has more sparsely distributed roughness elements. Sparseness of the roughness translates to a higher value of *Sk* as the mean surface height becomes relatively small compared to the maximum peak height, hence a more positively skewed surface height PDF. As Fig. 2 (bottom left) shows, for samples *Ia, Ib* and *III*, porosity becomes nearly zero at $y = 0$ meaning that the bottom wall is fully covered; this is not the case for sample *II*. Remarkably, when it comes to the s_f^* profiles, the maxima do not occur at $y = 0$. The reason is that, when the roughness elements are densely distributed, they overlap near the bottom plane and little free space remains among them. As a result, the extent of solid–fluid interface decreases and obviously there is a smaller flow fronting area. For sample *II*, the one with sparser roughness elements, the peak of s_f^* lies relatively close to the bottom wall indicating less overlapping. Comparing s_f^* of the two samples *Ia* and *Ib*, the latter reaches zero at a *y/H* half of the former due to the downscaling but its peak value is two times larger. It can be explained by the fact that the total roughness surface area remains constant despite downscaling[2] but this total area is confined to a smaller range of *y*, therefore the area density becomes larger. Indeed, it can be shown that the area underneath each s_f^* curve is equal to the frontal solidity of the corresponding surface. Frontal solidities are identical in all four samples.

4. Numerical solution

Pseudo-spectral in-house Navier–Stokes solver SIMSON (Chevalier et al., 2007) is used for both DNS and PFA simulations. For the present PFA simulations, same computational box as in Forooghi et al. (2017) is used; box dimensions in streamwise, wall-normal and spanwise direction are $(L_x, L_y, L_z) = (8H, H, 4H)$. Periodic boundary conditions are applied in both streamwise and spanwise directions. On the lower boundary of the box ($y = 0$), no-slip boundary condition is applied while at $y = H$, symmetry boundary condition is used (so-called open channel).

For the PFA simulations a grid of size $(N_x, N_y, N_z) = (768, 301, 384)$ nodes is used leading to a grid spacing of $(\Delta x, \Delta y, \Delta z)^+ \cong (5.5, 0.02 - 3.5, 5.5)$. A CFL number of 0.8 is used for time stepping, and the average (Runge–Kutta) time-step size is equal to roughly one-third of viscous time unit (ν/u_τ^2). For the calculation of statistics, temporal-averaging is carried out for at least 20 flow-through times after the statistical steady-state is reached. For calculation of certain statistical quantities (see Section 5) spatial averaging in wall-parallel directions over the entire domain is also applied. The spatial averaging is carried out over both fluid and solid parts of the domain, which is analogous to the 'superficial' averaging – a concept widely used in the porous media literature. In what follows, temporal and spatial averaging is denoted by overline $\overline{()}$ and angle brackets $\langle\,\rangle$, respectively.

5. Results and discussion

The model introduced in the previous section, contains model constants, whose values are not known a priori, thus, require 'calibration'. Based on the preliminary simulations with a wide parameter space, a range of c_D between 1.0 and 2.0 with k_K between 10 and 40 leads to satisfactory predictions and can be used for fine-tuning. In Section 5.1, a detailed discussion on the trends of flow statistics with

[2] Comparing *Ia* to *Ib* the surface area of each element in the latter is scaled down by a factor 1/4 but at the same time the total number of elements on the wall is 4 times larger.

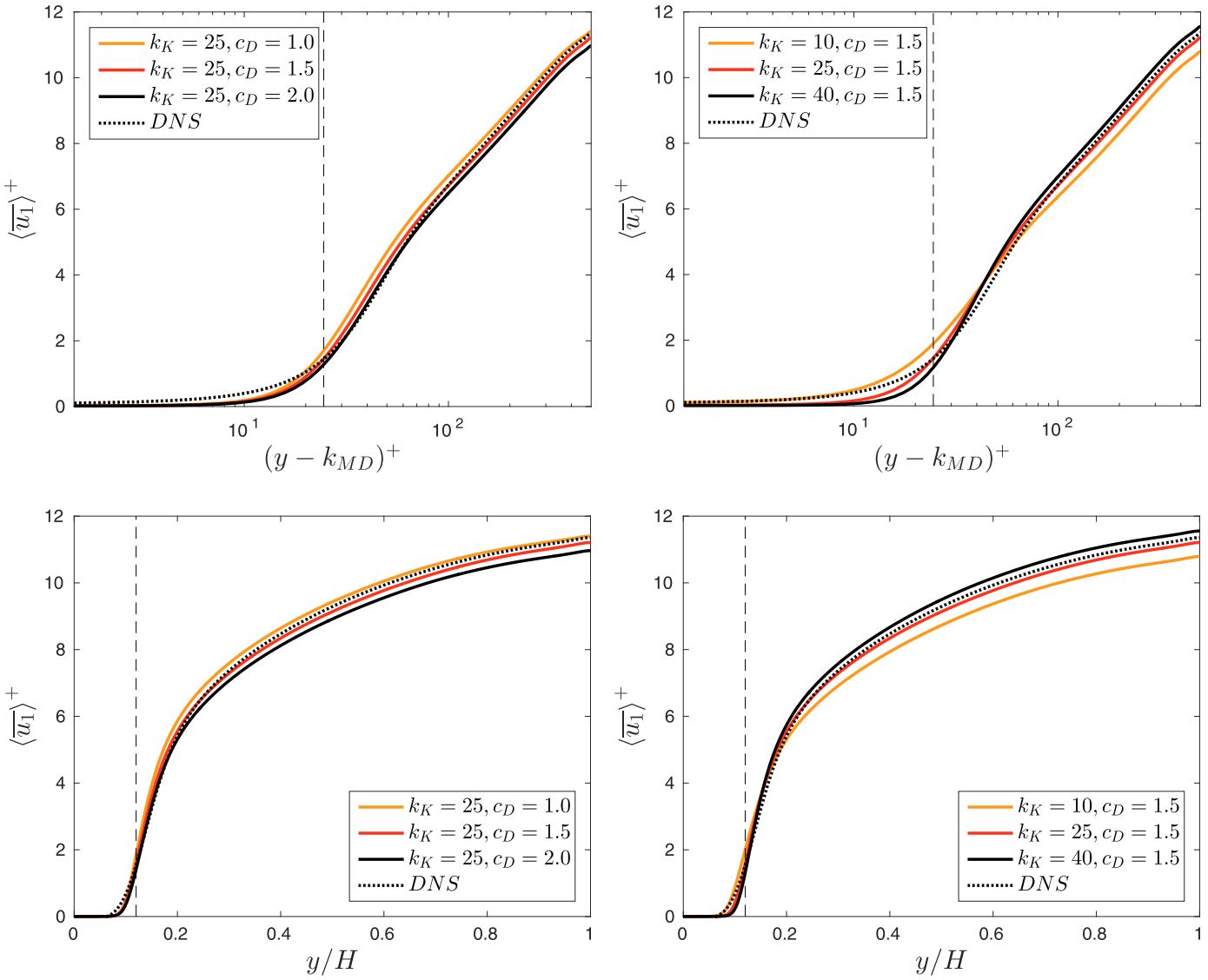

Fig. 3. Mean streamwise velocity profiles for sample *Ia* averaged over time and wall-parallel coordinates. Same profiles are plotted against inner-logarithmic (top) and outer-linear (bottom) *y*-coordinate. Left column: constant k_K, variable c_D; right column: constant c_D, variable k_K. Dotted line indicates DNS results for the same sample. Vertical dashed line indicates the mean roughness peak height.

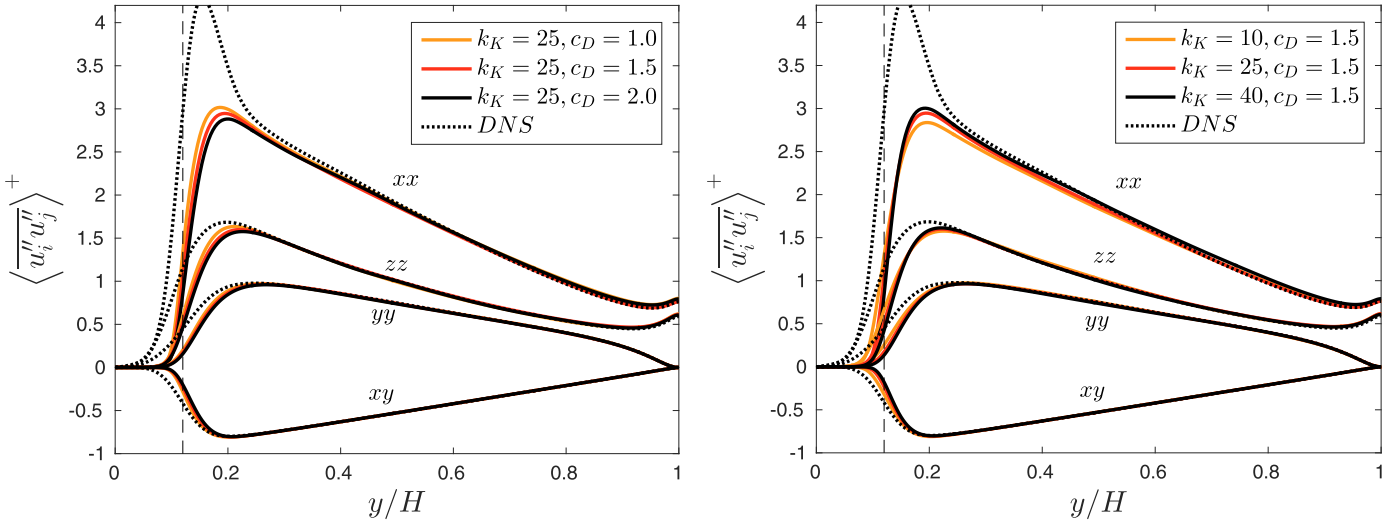

Fig. 4. Profiles of Reynolds stresses for sample *Ia* obtained from Eq. (16) in comparison with the DNS results for the same sample. Vertical dashed line indicates the mean roughness peak height.

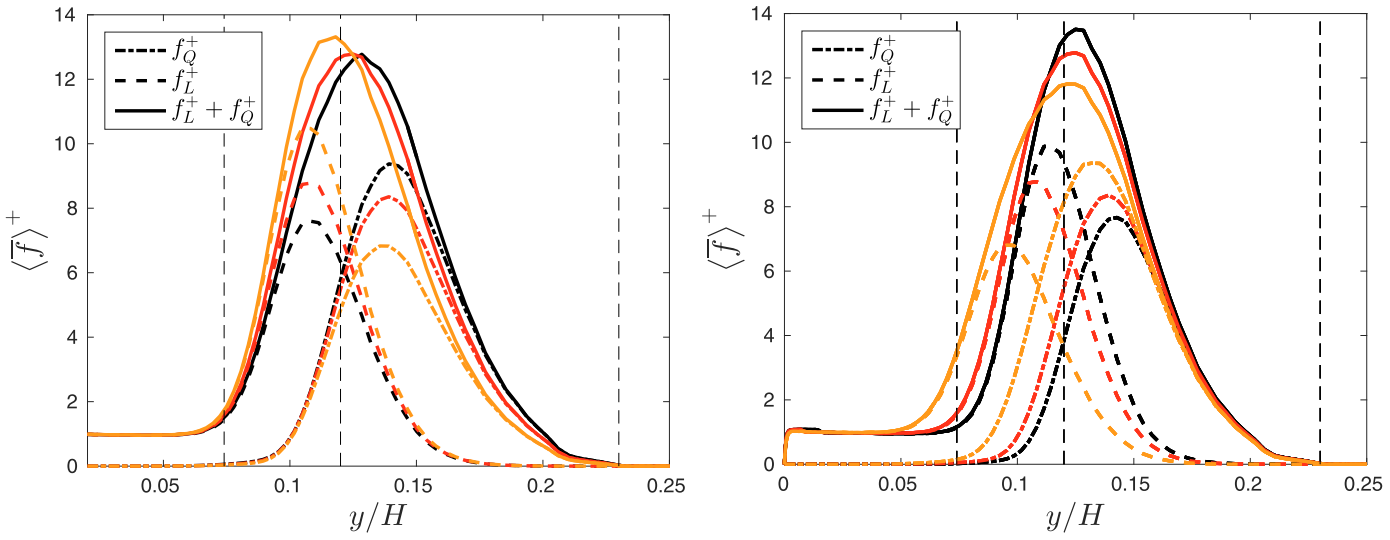

Fig. 5. Distribution of mean streamwise forcing term (solid line) and its linear (dashed line) and quadratic (dash-dotted line) components in the near wall region. Line colours in the left and right columns of the present figure have the same meaning as in the respective column of Fig. 3. Vertical dashed lines correspond to the horizontal dashed lines in Fig. 1, i.e. from left to right: melt down height ($y = k_{MD}$), mean peak height ($y = k$) and maximum peak height.

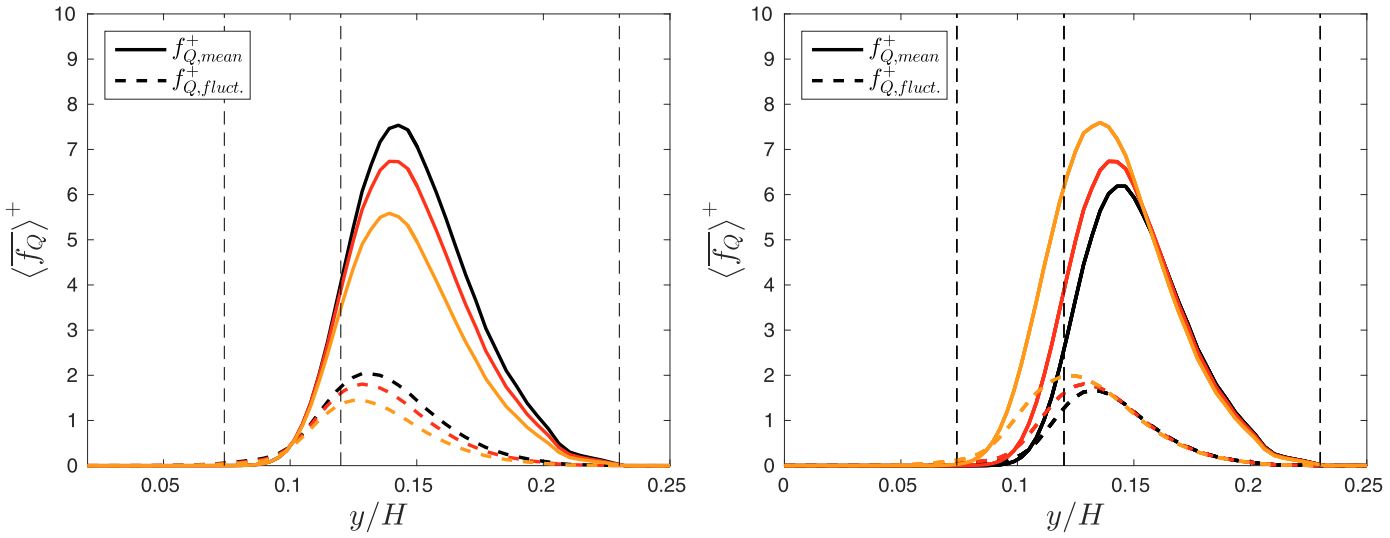

Fig. 6. Quadratic forcing term due to mean velocity (solid line) and fluctuations (dashed line). Either column of the present figure corresponds to the respective column of Fig. 5.

the model constants, in the above-mentioned range, is presented for one of the cases (*Ia*). In Section 5.2, the performance of the model for the other cases is examined. In this section one pair of the model constants based on in Section 5.1 is adopted.

5.1. Effect of model constants

Fig. 3 shows the effect of the model constants in the ranges $1.0 \leq c_D \leq 2.0$ and $10 \leq k_K \leq 40$ on the calculated mean velocity profile in comparison to the corresponding DNS simulation (dotted line). In general, the agreement between the DNS and PFA results are satisfactory over the entire range. It can be observed in the logarithmic plots that both an increase in c_D and a decrease in k_K lead to a downward shift in the logarithmic region or, in other words, an increased roughness function. The logarithmic behaviour itself is not affected by the choice of the constants; in all cases the logarithmic region starts at $(y - k_{MD})^+ \cong 50$.

The downward trend of velocity profile with c_D is an expected behaviour since the resistance to the flow is in direct relation to c_D. The explanation of the trend with k_K is, however, less straightforward as the resistance increases with an increase in this constant. Indeed, in the region closer to $y = 0$ where, as will be shown later, the linear forcing term dominates, an increase in k_K, as expected, suppresses the flow; however, the suppression of flow in this region entails a lower flow in the entire roughness layer, thus, a less intense quadratic forcing. The overall effect is a steeper velocity profile towards the edge of the roughness layer, and an upward shift in the neighbouring logarithmic region. One should pay attention to the fact that the 'inflection point', which is typical of the mean velocity profiles near the roughness crest, remains almost at the same location with the variation of k_K. At this point it is possible to explain why the linear forcing term is required for a reasonable prediction of the velocity profile. In the absence of this term, the resistance in the region near the wall would be underpredicted by the quadratic term, resulting in an increased velocity and, thus, form drag near the edge of the roughness layer and consequently, an overprediction of the roughness function. To avoid this overprediction, a smaller value of c_D should be used, which leads to a high deviation from the physical velocity profile in the buffer layer. In

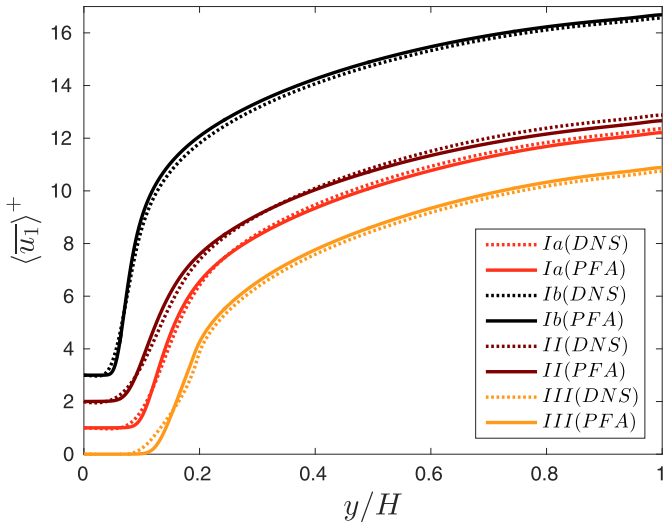

Fig. 7. Mean streamwise velocity profiles of all cases obtained from PFA (solid line) in comparison to DNS (dashed line) results.

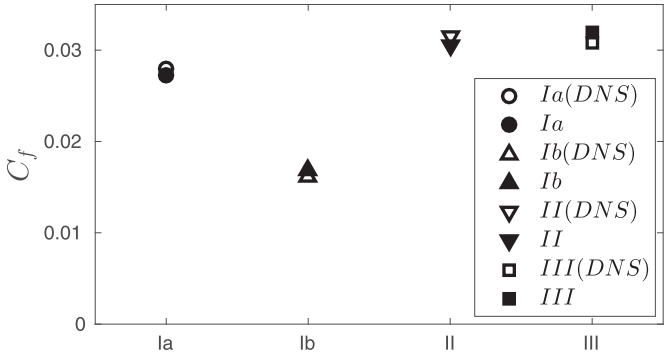

Fig. 8. The predicted values of friction factor by PFA (filled symbols) and DNS (hollow symbols) for all cases.

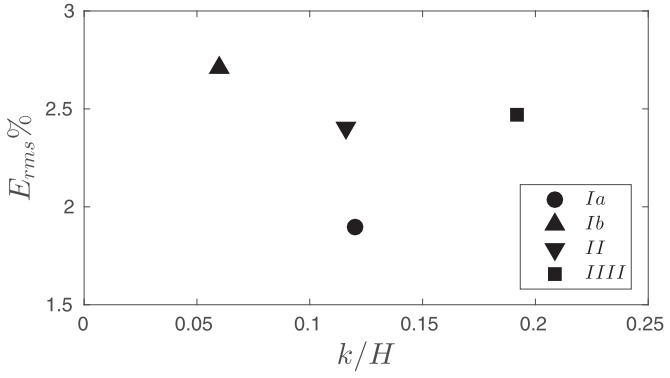

Fig. 9. Rms error in the prediction of mean velocity profile by PFA in comparison to DNS; roughness characteristic dimension is used as abscissa variable.

summary, it is possible to match the value of either the bulk velocity or roughness function using a single constant c_D, but the velocity profile – particularly in the neighbourhood of the roughness crest – could not be captured correctly if $k_K = 0$. It is observed that the present model could not correctly match the profile in the very vicinity of the reference plane, i.e. $(y - k_{MD})^+ < 15$, , but since this region accounts for a very small portion of the flow rate, this deviation can be tolerated.

As already pointed out, the model is mainly designed to predict the mean velocity profile and, consequently, the friction factor. However, a comparison of the most influential turbulence statistics is instructional. Such a comparison is made for the Reynolds stresses in Fig. 4. Here, the fluctuating velocity u_i'' used to define the Reynolds stresses, is obtained by calculating the difference between the local instantaneous velocity and the double averaged mean, i.e. $u_i'' = u_i - \langle \overline{u_i} \rangle$. As a result of homogeneity in the wall-parallel directions in PFA, the same result would be achieved if only temporal averaging were used for the calculation of the fluctuations, provided that the averaging time is long enough. In the reality (DNS), however, the fluctuating component u_i'' can be further decomposed into a time-invariant component $\widetilde{u_i}$, representing the spatial deviation from $\langle \overline{u_i} \rangle$, and a temporal fluctuating component u_i'. As a result, $\langle \overline{u_i'' u_j''} \rangle$ could be expressed as

$$\langle \overline{u_i'' u_j''} \rangle = \langle \overline{u_i' u_j'} \rangle + \langle \widetilde{u_i} \widetilde{u_j} \rangle \tag{16}$$

The first term on the right hand side is the true Reynolds stress, and the second term on the right hand side is referred to as 'dispersive stress'. Details on the computation of the dispersive stresses in DNS are provided in Appendix A. Further discussions on the meaning and role of dispersive stresses can also be found in Coceal et al. (2006) and De Marchis et al. (2010). In the present – and any 'homogenized' modelling approach – dispersive stress is zero and there is no distinction between $\langle \overline{u_i'' u_j''} \rangle$ and $\langle \overline{u_i' u_j'} \rangle$. This issue will be discussed further in Section 5.2. Here we mainly focus on the effect of model constants on the Reynolds stresses calculated from the model results. It is clear in Fig. 4 that variations of both model constants mainly influence the peak values of Reynolds stress profiles and the region below it. A decrease in c_D and an increase in k_K both lead to a higher peak value. This agrees well with the trend of mean velocity and suggests that the modelled peak value is related to the mean velocity gradient in the vicinity of the peak location, i.e. slightly above the edge of the roughness layer. The modelled Reynolds stress profiles all collapse with the profile of $\langle \overline{u_i'' u_j''} \rangle$ towards the middle of the channel, which agrees well with the outer layer similarity hypothesis. In the near wall region, however, the agreement is poor, particularly for the *xx* component of the Reynolds stress. This can be attributed to the simplifications in the physics of the problem made by the model.

So far, the influence of the model constants on the flow statistics is discussed. It is insightful to additionally observe how the linear and quadratic forcing terms reflect a variation in either constants. For that purpose, Fig. 5 shows the wall-normal double averaged profiles of these two terms along with their sum. Here only the region below the roughness crest where f_i assumes non-zero values is shown, and only the streamwise direction is discussed. For brevity index $i = 1$ is dropped. The graph on the left hand side presents the results from constant k_K but variable c_D and the one on the right hand side presents those with constant c_D but variable k_K (similar to the left and right columns in Fig. 3, respectively). For better comparison, the locations of melt-down plane ($y = k_{MD}$), mean roughness peak height ($y = k$) and roughness crest are indicated by vertical dashed lines in both graphs. It is observed that the linear and quadratic forcing terms dominate in the region below and above $y = k$, respectively. Total force peaks in the area around $y = k$ where both terms are present. As expected, an increase in the model constant related to each term, increases the share of the respective term in the total drag. The peak location of either term shows little sensitivity to the variation of the model constant. It can be understood that the centroid of the drag profile adjusts itself more to the geometry and less to the values of the model constants.

One should note that both mean and fluctuating velocities are present in the quadratic forcing term. For $i = 1$, assuming that $u_1 > 0$:

$$\langle \overline{f_{Q,1}} \rangle^+ = B^+ \langle \overline{u_1} \rangle^{+2} + B^+ \langle \overline{u_1''^2} \rangle^+ \tag{17}$$

The distinction between the two components is important for example in the context of turbulence modelling where the momentum equation is solved only for the mean velocity and any effect of the fluctuations needs to be accounted for through closure equations. Fig. 6 compares the first (solid line) and second (dashed line) terms on the right hand

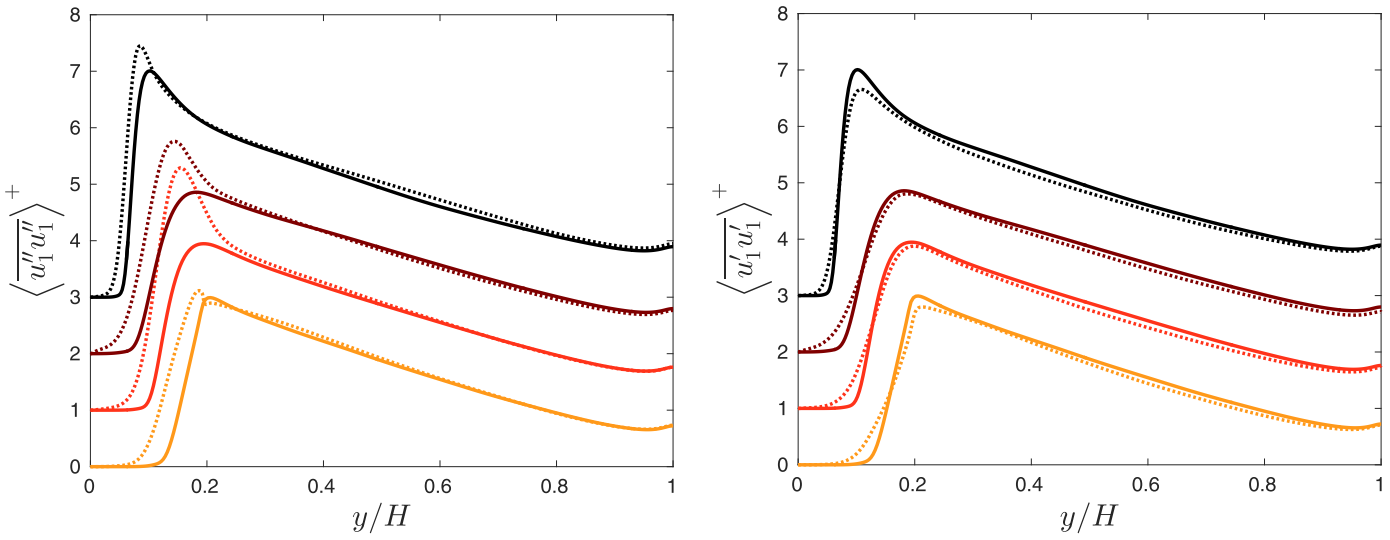

Fig. 10. Profiles of Reynolds stress (*xx* component) calculated by PFA for all cases in comparison with the profiles of total turbulent (left) and Reynolds stress (right) from DNS (Reynolds stress = total stress − dispersive stress). Line legend is same as in Fig. 7.

side of Eq. (17). It is observed that for the case under consideration the fluctuating term only accounts for approximately 20% of the 'modelled' form drag. It is also revealed that both components show similar trends to the variation of the model constants.

5.2. Evaluation of the model

In the present section the simulation results of all cases obtained with the constant values of $k_K = 25$ and $c_D = 1.5$, those delivering the smallest deviation from the DNS solution for case *Ia*, are discussed. The orders of magnitude of these model constants match those of Kozney constant and drag coefficient in similar problems therefore is physically justified.

Mean velocity profiles from all samples introduced in Table 1 are presented in Fig. 7 along with the same profiles obtained from DNS. For visual reasons, profiles of cases *Ia, II* and *Ib* are shifted upwards by 1, 2 and 3 units, respectively. A very good agreement with DNS is observed in all cases. Similar to what already observed for case *Ia*, there is a slight deviation around the point where velocity starts to grow from zero. Having said that, the general shape of the profiles and, in particular, the location of the inflection point is reproduced well by the model. Also the values of friction factor calculated from the PFA agree well with those from DNS as shown in Fig. 8. This figure demonstrates how the present model is able to predict the trends of friction factor with topographical surface properties, i.e. *Sk* (compare *Ia* and *II*) and Δ (compare *Ia* and *II*) as well as the characteristic roughness height (compare *Ia* and *Ib*).

It should be recalled that the purpose of the present approach is not only to predict the friction factor correctly, but also to reproduce the mean velocity profile as closely as possible. To better quantify the latter capability, the root-mean-square error of the calculated velocity profiles compared to the DNS profiles defined as

$$E_{rms} = \frac{\sqrt{\int_0^H (\langle \overline{u_{1,PFA}} \rangle - \langle \overline{u_{1,DNS}} \rangle)^2 dy}}{\int_0^H \langle \overline{u_{1,DNS}} \rangle dy} \tag{18}$$

are calculated and displayed in Fig. 9. The figure reveals that the root-mean square error is less than 3% for all cases.

Finally, the computed profiles of Reynolds stress are shown in Fig. 10. Only the most critical component, i.e. the *xx* component is discussed here. On the left column (similar to Fig. 4) the profiles of $\langle \overline{u_1'' u_1''} \rangle$ from DNS are added for comparison, while on the right column only the pure Reynolds stress, i.e. $\langle \overline{u_1' u_1'} \rangle$ from DNS is presented. As already reasoned, there is no difference between these two quantities in PFA.

As previously observed in the results of sample *Ia* in Section 5.1, Fig. 10 (left) shows that PFA meaningfully underpredicts the peak of $\langle \overline{u_1'' u_1''} \rangle$ for all cases. This underprediction is most severe for case *II* and least for case *III*. Moreover, $\langle \overline{u_1'' u_1''} \rangle$ from PFA is damped abruptly inside the roughness layer, while DNS shows higher values below the roughness crest. However, if the dispersive stresses are taken away from $\langle \overline{u_1'' u_1''} \rangle$ and only the pure Reynolds stress $\langle \overline{u_1' u_1'} \rangle$ is considered, a different picture is obtained. As shown in Fig. 10 (right), in this case the agreement between the PFA and DNS improves significantly. Unlike for $\langle \overline{u_1'' u_1''} \rangle$, the peak of $\langle \overline{u_1' u_1'} \rangle$ is slightly overpredicted by PFA, suggesting that the extra amount that the model is not able to reproduce in the former case, is due to the dispersive stress. Physically speaking, dispersive stresses find no counterpart in a 'homogenized' roughness approach like the present one, and their absence in the calculated flow field by the model is sensible. Case *Ib*, which has the lowest k^+ value among all, shows the largest amount of deviation in its predicted peak value. In the prediction of Reynolds stress $\langle \overline{u_1' u_1'} \rangle$ – similar to the mean velocity profile – the present model produces a sharper transition from the near-wall motionless fluid to the flow above it and, as a result, an underprediction inside the roughness layer. The deviation inside this layer is however less pronounced than for $\langle \overline{u_1'' u_1''} \rangle$ as the dispersive stress part is not present.

6. Conclusion

A modified version of the Parametric Forcing Approach (PFA) for modelling of surface roughness is suggested and tested for prediction of flow in so-called open channel configuration for four dense roughness samples with different morphological surface properties. The results are compared to the already available full-geometry resolved DNS results for the same geometries at the same friction Reynolds number ($Re_\tau \cong 500$). The model is based on adding two source terms (forcing terms) to the otherwise-unchanged incompressible momentum equation. The two forcing terms are linearly and quadratically related to the local instantaneous velocity, representing the viscous and form drag effects of the roughness features. The model includes two model constants analogous to Kozney constant (k_K) and drag coefficient (c_D). Based on the analysis of the results the following points are understood:

– The PFA model is able to reproduce both friction factor and mean velocity profile from full-geometry resolved DNS with the model

constant values $c_D = 1.5$ and $k_K = 25$. The presence of the linear forcing term improves the capability of the model for capturing the mean velocity profile. The root-mean-square error in the prediction of the mean velocity profile is less than 3% for the investigated cases.
- The effects of the investigated morphological surface properties, i.e. the skewness of surface height PDF and the coefficient of variation of peak heights, are well reproduced by the model.
- The total forcing term peaks in the vicinity of the mean roughness peak height plane, and the peak location shows little sensitivity to the values of the model constants.
- Reynolds stresses are sensitive to the choice of model constants only in the vicinity of the roughness and collapse well in the outer layer irrespective of the model constants.
- The model is able to reproduce the profiles of Reynolds stress from DNS relatively well with some underprediction in the peak values. This underprediction is more severe for the case of transitionally-rough regime. Having said that, the model is unable to reproduce the dispersive stresses due to spatial inhomogeneity of the flow near the rough surface. Consequently, when the profiles of Reynolds stress from the model is compared to the sum of Reynolds and dispersive stresses from DNS, a considerable underprediction is observed within the roughness sublayer.

In view of the above, we believe that a proof of concept for a modified PFA model, which is capable of predicting the mean flow for an arbitrary roughness geometry, is in hand. The model will obviously benefit from further verification and possible refinements. Further work on the model is suggested in two directions; comparison to the experimental data at higher Reynolds numbers for the prediction of friction coefficient and comparison to other independent full-geometry resolved DNS for the prediction of mean velocity profile and possibly turbulence statistics. Comparison to the results obtained from realistic roughness will be particularly advantageous.

Acknowledgements

PF, BF and FM acknowledge financial support by the German Research Foundation (DFG) under Collaborative Research Centre SFB/TRR150. AB acknowledges financial support by the Engineering and Physical Sciences Research Council (grant number EP/P004687/1). The computations for this research were carried out on HPC cluster ForHLR2 at Karlsruhe Institute of Technology. PF thanks Karlsruhe House of Young Scientists for financing a research visit to University of Glasgow, which made the present collaboration possible.

Appendix A

The velocity field $u_i(x, y, z, t)$ can be decomposed into a temporally-averaged and a fluctuating components, i.e.

$$u_i(x, y, z, t) = \overline{u}_i(x, y, z) + u_i'(x, y, z, t) \tag{A1}$$

where overbar indicates temporal averaging. Time-averaged velocity $\overline{u}_i(x, y, z)$ can be further averaged spatially in x and z-directions, and be decomposed into two components, i.e.

$$\overline{u}_i(x, y, z) = \langle \overline{u}_i \rangle(y) + \tilde{u}_i(x, y, z) \tag{A2}$$

where angle brackets indicate spatial averaging in x and z-directions. Consequently, Eq. (A1) can be rewritten as:

$$u_i(x, y, z, t) = \langle \overline{u}_i \rangle(y) + \tilde{u}_i(x, y, z) + u_i'(x, y, z, t) \tag{A3}$$

It should be noted that if the turbulence is homogeneous in x and z-directions, $\overline{u}_i$ is only a function of y, so the second term on the right hand side of Eq. (A3) vanishes once the statistics are converged (hereinafter the independent variables are dropped in all expressions for brevity).

In the present study, we compute $\overline{u}_i$ and $\overline{u_i u_j}$ by temporal averaging on the fly. This makes possible local computation of the Reynolds stresses in post processing using

$$\overline{u_i' u_j'} = \overline{u_i u_j} - \overline{u}_i \overline{u}_j. \tag{A4}$$

Reynolds stresses can be further averaged spatially to obtain the y-dependent profiles of $\langle \overline{u_i' u_j'} \rangle$ plotted in Fig. 10.

For the computation of dispersive stresses, one can calculate $\langle \overline{u}_i \rangle$ and $\langle \overline{u_i u_j} \rangle$ by spatial averaging of already available $\overline{u}_i$ and $\overline{u_i u_j}$ fields. One can show that

$$\langle \overline{u_i'' u_j''} \rangle = \langle \overline{u_i u_j} \rangle - \langle \overline{u}_i \rangle \langle \overline{u}_j \rangle \tag{A5}$$

where u_i'', already introduced in the text, denotes sum of $\tilde{u}_i$ and u_i'. Dispersive stresses can be calculated by subtracting $\langle \overline{u_i' u_j'} \rangle$ from $\langle \overline{u_i'' u_j''} \rangle$ according to Eq. (16).

References

Anderson, W., Meneveau, C., 2010. A large-eddy simulation model for boundary-layer flow over surfaces with horizontally resolved but vertically unresolved roughness elements. Boundary Layer Meteorol. 137 (3), 397–415.
Bhaganagar, K., 2008. Direct numerical simulation of unsteady flow in channel with rough walls. Phys. Fluids 20 (10), 101508. (1994–present).
Busse, A., Lützner, M., Sandham, N.D., 2015. Direct numerical simulation of turbulent flow over a rough surface based on a surface scan. Comput. Fluids 116, 129–147.
Busse, A., Sandham, N.D., 2012. Parametric forcing approach to rough-wall turbulent channel flow. J. Fluid Mech. 712, 169–202.
Chan, L., MacDonald, M., Chung, D., Hutchins, N., Ooi, A., 2015. A systematic investigation of roughness height and wavelength in turbulent pipe flow in the transitionally rough regime. J. Fluid Mech. 771, 743–777.
Chevalier, M., Schlatter, P., Lundbladh, A., Henningson, D.S., 2007. SIMSON – A Pseudo-Spectral Solver for Incompressible Boundary Layer Flow. Technical Report. KTH.
Choi, H., Moin, P., Kim, J., 1993. Direct numerical simulation of turbulent flow over riblets. J. Fluid Mech. 255, 503–539.
Coceal, O., Thomas, T., Castro, I., Belcher, S., 2006. Mean flow and turbulence statistics over groups of urban-like cubical obstacles. Boundary Layer Meteorol. 121 (3), 491–519.
Cui, J., Patel, V.C., Lin, C.-L., 2003. Prediction of turbulent flow over rough surfaces using a force field in large eddy simulation. J. Fluids Eng. 125 (1), 2–9.
De Marchis, M., Napoli, E., Armenio, V., 2010. Turbulence structures over irregular rough surfaces. J. Turbul. (11), N3.
Flack, K.A., Schultz, M.P., 2010. Review of hydraulic roughness scales in the fully rough regime. ASME J. Fluids Eng. 132 (4), 041203.
Forooghi, P., Stroh, A., Magagnato, F., Jakirlić, S., Frohnapfel, B., 2017. Toward a universal roughness correlation. J. Fluids Eng. 139 (12), 121201.
Hama, F.R., 1954. Boundary layer characteristics for smooth and rough surfaces. Trans. Soc. Nav. Arch. Marine Eng. 62, 333–358.
Jimenez, J., 2004. Turbulent flows over rough walls. Annu. Rev. Fluid Mech. 36, 173–196.
Kaviany, M., 1995. Principles of Heat Transfer in Porous Media, Second edition. Springer.
Lācis, U., Bagheri, S., 2017. A framework for computing effective boundary conditions at the interface between free fluid and a porous medium. J. Fluid Mech. 812, 866–889.
Mazzuoli, M., Uhlmann, M., 2017. Direct numerical simulation of open-channel flow over

a fully-rough wall at moderate relative submergence. J. Fluid Mech. 824, 722–765.
Napoli, E., Armenio, V., De Marchis, M., 2008. The effect of the slope of irregularly distributed roughness elements on turbulent wall-bounded flows. J. Fluid Mech. 613, 385–394.
Nikuradse, J., 1933. Strömungsgesetze in rauen Rohren. VDI-Forschungsheft 361.
Orlandi, P., Leonardi, S., 2006. DNS of turbulent channel flows with two- and three-dimensional roughness. J. Turbul. 7 (53), N73.
Ozgumus, T., Mobedi, M., Ozkol, U., 2014. Determination of kozeny constant based on porosity and pore to throat size ratio in porous medium with rectangular rods. Eng. Appl. Comput. Fluid Mech. 8 (2), 308–318.
Schultz, M.P., Flack, K.A., 2009. Turbulent boundary layers on a systematically varied rough wall. Phys. Fluids 21, 015104.
Tarada, F., 1990. Prediction of rough-wall boundary layers using a low reynolds number k-epsilon model. Int. J. Heat Fluid Flow 11 (4), 331–345.
Taylor, R., Coleman, H., Hodge, B., 1985. Prediction of turbulent rough-wall skin friction using a discrete element approach. J. Fluids Eng. 107 (2), 251–257.
Thakkar, M., Busse, A., Sandham, N., 2017. Surface correlations of hydrodynamic drag for transitionally rough engineering surfaces. J. Turbul. 18 (2), 138–169.
Vafai, K., Kim, S., 1995. On the limitations of the Brinkman–Forchheimer-extended Darcy equation. Int. J. Heat Fluid Flow 16 (1), 11–15.
Yuan, J., Piomelli, U., 2014. Estimation and prediction of the roughness function on realistic surfaces. J. Turbul. 15 (6), 350–365.